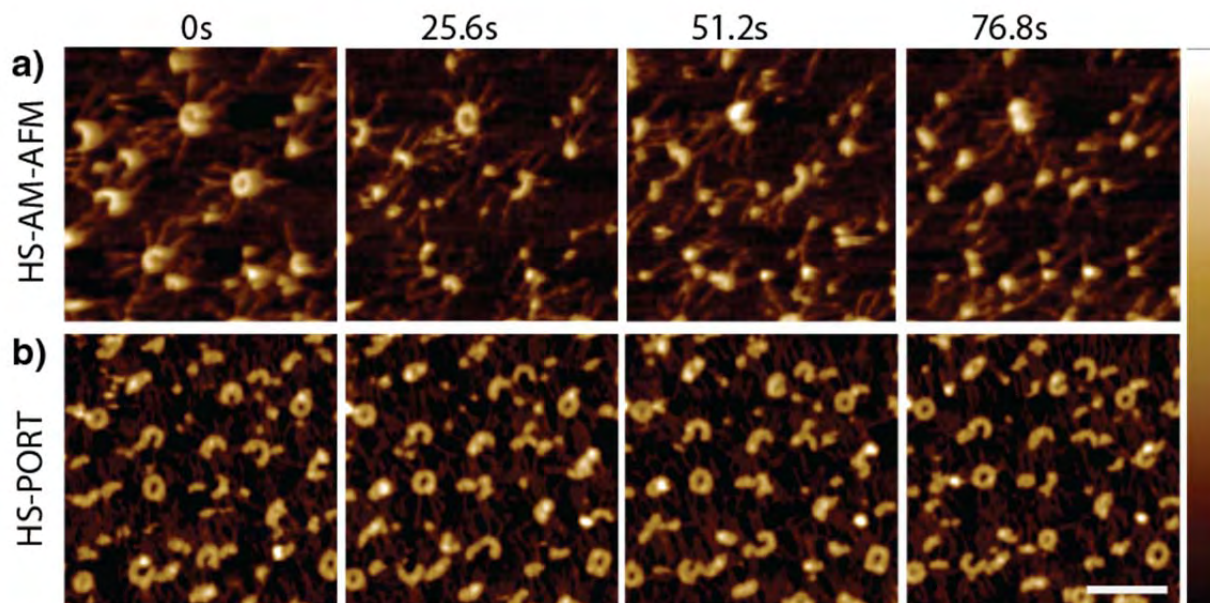


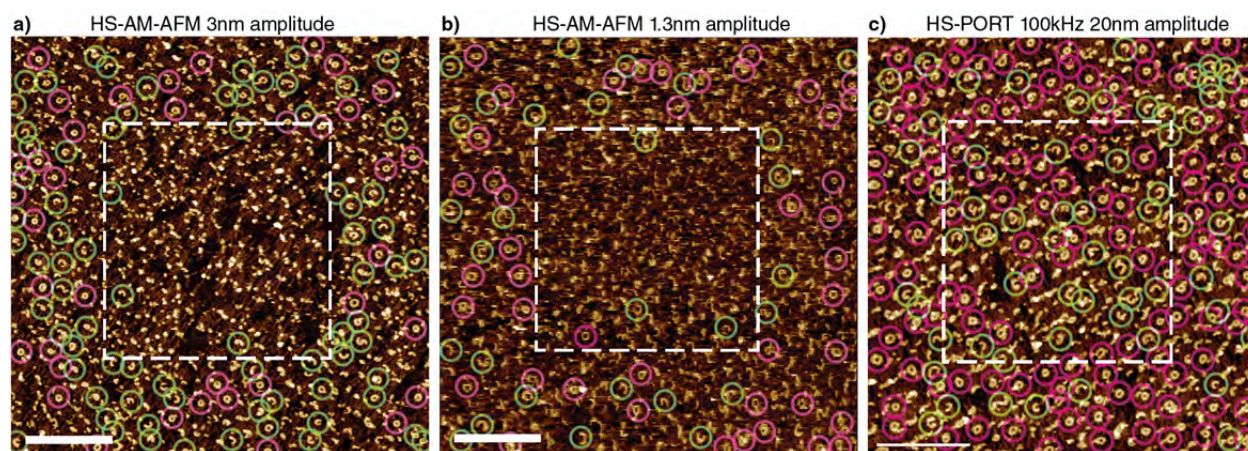
Supplementary Information: High-speed photothermal off-resonance atomic force microscopy reveals assembly routes of centriolar scaffold protein SAS-6

Adrian P. Nievergelt, Niccolò Banterle, Santiago H. Andany, Pierre Gönczy and Georg E. Fantner

1. Disruption of fully formed rings in AM-AFM



Supplementary Fig. 1: Assessment of sample damage induced by imaging. a) Continuous imaging of pre-formed CrSAS-6 rings with HS-AM-AFM leads to ring disassembly (top row, one frame every 10 frames shown). b) HS-PORT imaging with the same rate showed no sign of induced damaging over the observed time period (bottom row). Scale bar is 100nm, z-scale is 0-6.3nm.



Supplementary Fig. 2: Comparison of HS-AM-AFM imaging of CrSAS-6 ring assembly under different imaging parameters. Overview of the imaging area (dashed square) and the surrounding region of CrSAS-6 assembly on Mica after continuous

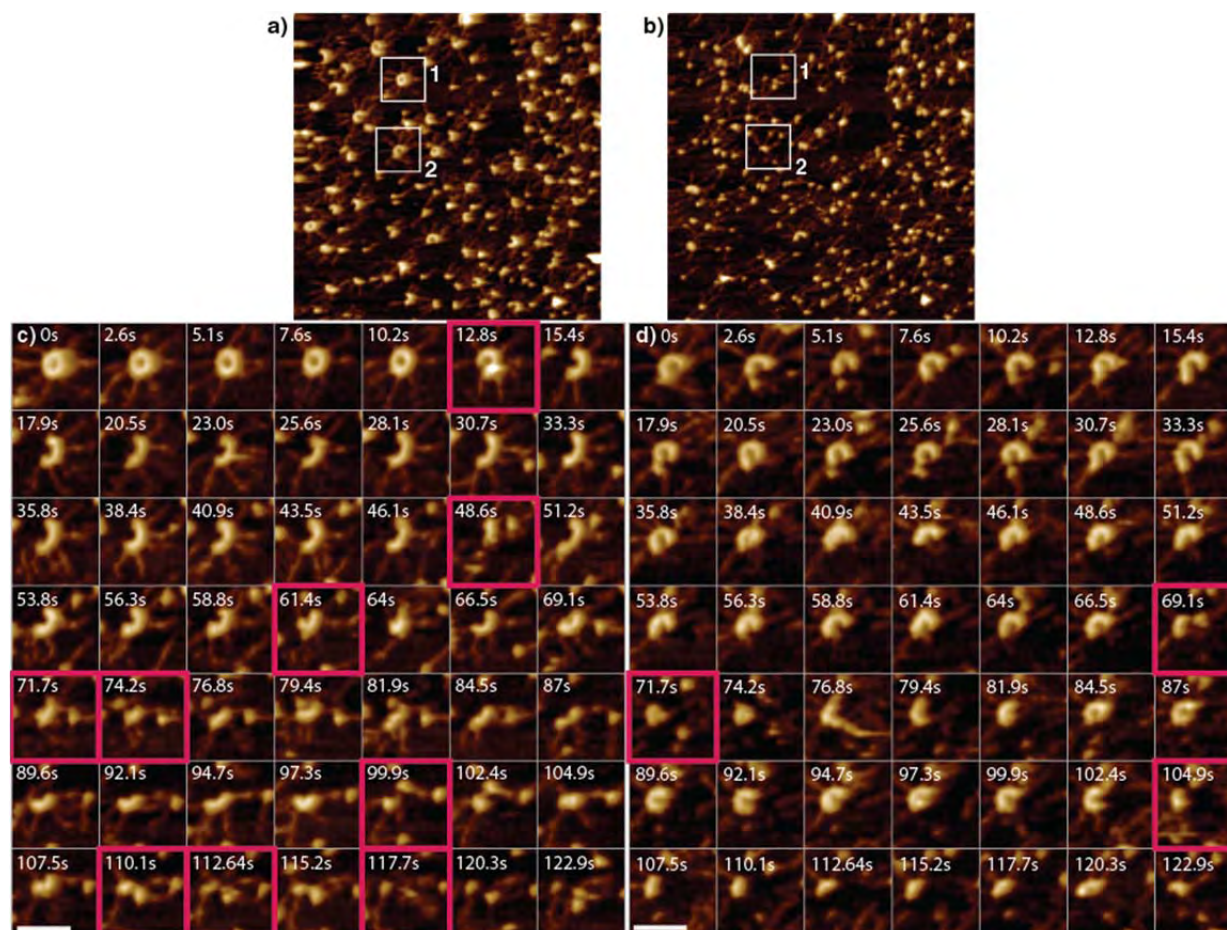
15 *imaging at equilibrium for: a) HS-AM-AFM with 3nm amplitude, 86% set point b) HS-AM-AFM with 1.3 nm amplitude and 90%*
16 *set point c) HS-PORT with 100kHz and 20nm amplitude. While both HS-AM-AFM images show significant disruption of higher*
17 *order oligomers, in HS-PORT there is no significant change between the scanned area and the surrounding area (see **Error!***
18 ***Reference source not found.***).

19

Comparison of ring-counts for different techniques

	$C_{partial}^{out}$	C_{full}^{out}	$C_{partial}^{in}$	C_{full}^{in}	$C_{partial}^{in}/C_{partial}^{out}$	$C_{full}^{in}/C_{full}^{out}$
	μm^{-2}	μm^{-2}	μm^{-2}	μm^{-2}	%	%
HS-AM-AFM 3nm	53.3	28.1	6	0	11.3 ($p = 0.0047$)	0 ($p < 0.001$)
HS-AM-AFM 1.3nm	19.2	31.8	4.9	1.6	25.5 ($p = 0.0015$)	5 ($p < 0.001$)
HS-PORT 100kHz 20nm	28	67	41	46	146.4 ($p=0.25$)	68.65 ($p=0.068$)

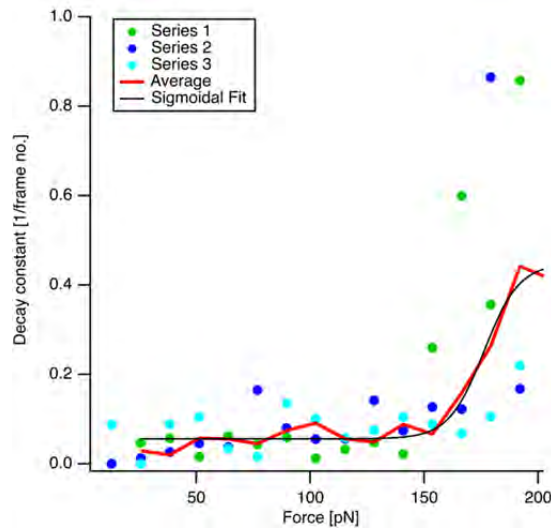
Supplementary Tab. 1: Surface density of CrSAS-6 partial and full ring assemblies both in the scan area and in the surrounding area for different parameters, showing the significant imaging damage induced by HS-AM-AFM imaging during formation. In comparison, HS-PORT does not induce significant changes. p values were calculated as $P(C^{out} = C^{in})$ assuming counting (Poisson) statistics.



Supplementary Fig. 3: Representative cropped frame-by-frame series of SAS-6 oligomers breaking during imaging in HS-AM-AFM, from supplemental movie 2. a) Overview of first frame and b) last frame, highlighting the zoom-in areas 1 and 2, corresponding to panels c) and d), respectively. Red boxes highlight frames where a significant disruption of the oligomer is visible relative to the previous frame. Scale bar is 30nm, z scale is 6.3nm, like in supplemental figure 1.

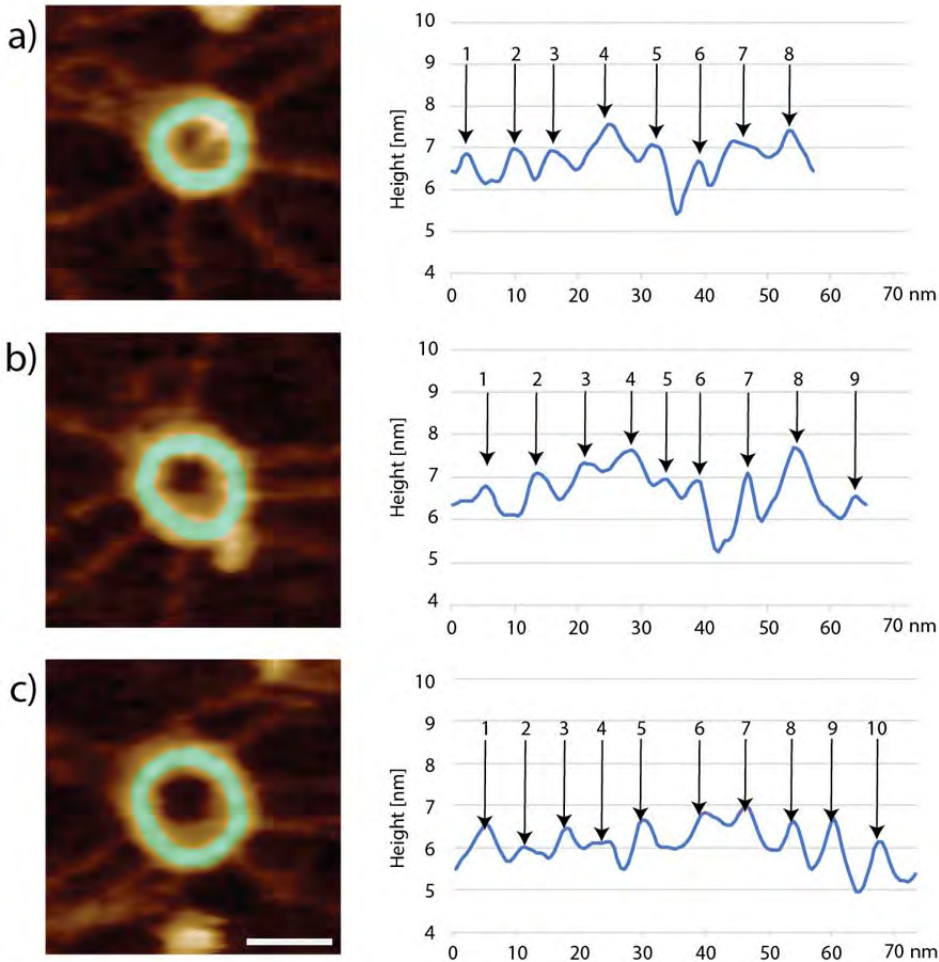
To assess the influence of imaging force on ring stability, we imaged fully assembled CrSAS-6 rings on Mica in HS-PORT at increasing force set points ($f_m = 100\text{kHz}$). For each set point force a fresh scan area with >15 fully assembled rings was observed for over 10 frames. The decay of full rings over time was then assessed by extracting the breaking probability. This was done by counting the rings that remained intact, and fitting the resulting counts with an exponential decay. The resulting decay constants

averaged over three sets of experiments (Supplemental Figure 2) shows non-negligible breaking after 150pN.



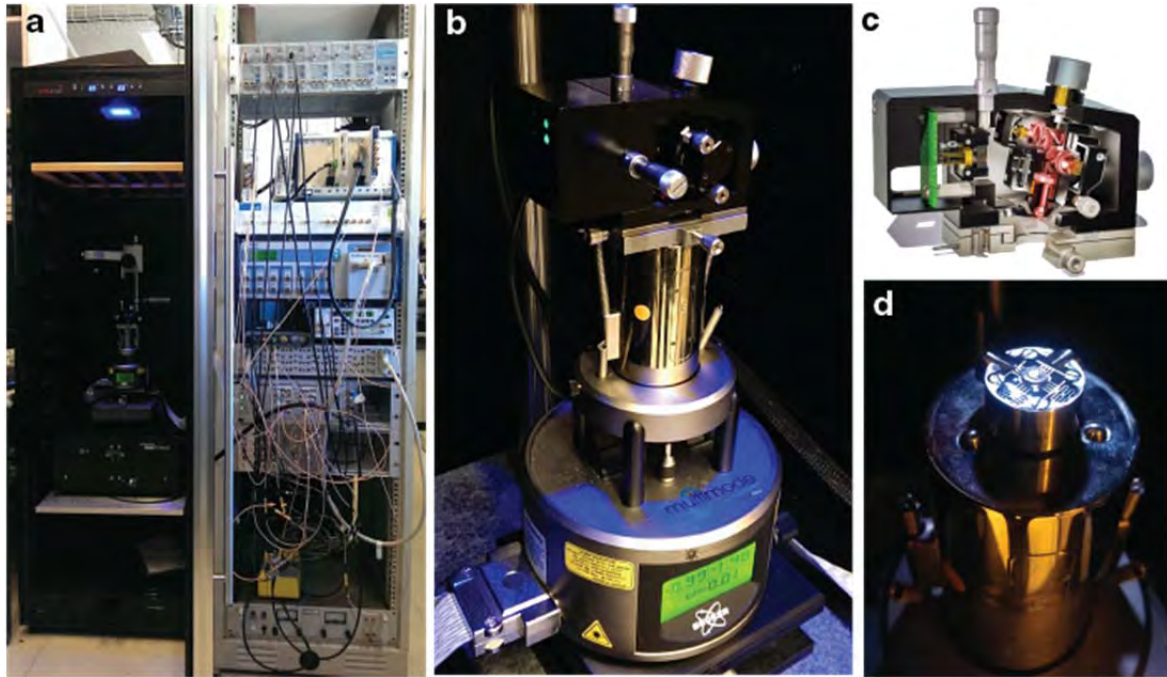
Supplementary Fig. 4: Rates of disassembly induced by continuous imaging of CrSAS-6 rings at increasing forces. Fields of view of pre-formed rings were continuously imaged, and the number of rings never opening (N) were counted in successive frames (up to ten frames). The decay constant was extracted from an exponential fit of N over frames. The decay constant was measured at different force set point in three independent experiments (blue, cyan and green bullets). The average decay curve (red solid line), fitted with a sigmoidal function, shows that significant imaging induced ring opening is detectable from 150pN on, and rapidly increases thereafter.

2. High-resolution imaging of SAS-6 in PORT



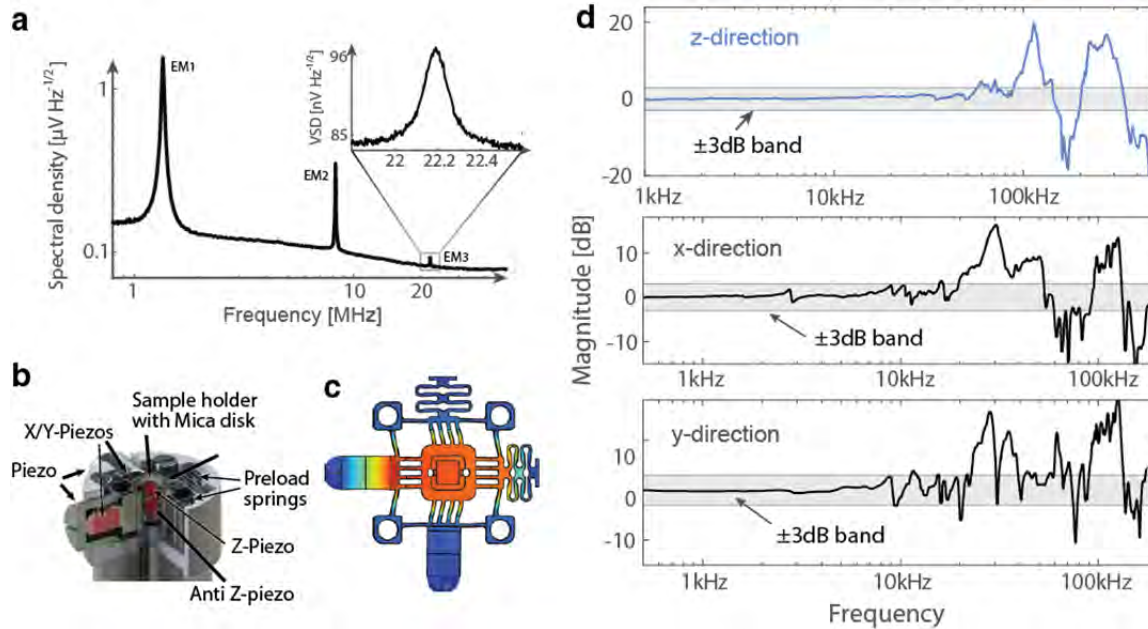
Supplementary Fig. 5: High resolution images of fully formed CrSAS-6 rings (left) and corresponding height profiles extracted along the rings (green overlay in images, arc lengths represented on the X axes) for assemblies with a) 8 homodimers, b) 9 homodimers and c) 10 homodimers. The number of homodimers can be clearly discerned by the number of peaks.

3. Home-built atomic force microscope



Supplementary Fig. 6: Home-built high-speed atomic force microscope. a) Full setup showing the AFM head, base scanner and isolation table inside the wine cooler. b) The microscope is compatible with the widespread MultiMode (Bruker Nano). The head is attached to the translation stage with magnets to facilitate quick turnover of experiments. c) Internal light path of the microscope head. The readout laser and the drive laser are combined internally, but the drive laser can be adjusted relative to the readout laser. d) A custom, small-scale high-speed scanner based on a flexure design provides $1.8\mu\text{m} \times 1.8\mu\text{m} \times 2\mu\text{m}$ of scan range at a closed loop z-bandwidth of more than 60kHz.

The homebuilt system represents improvements of the long established MultiMode AFM system. Previously, we have reported head designs for improved spot size, allowing for smaller cantilevers¹, as well as the possibility to use photothermal drive², which provides clean and fast excitation in any environment. In our latest revision of this head, we have improved the laser positioning mechanics and further reduced the spot size in order to be able to utilize cantilevers with a width below $2\mu\text{m}$. The small spot size in combination with a custom translinear photodiode readout³ enables us to detect up to the third Eigenmode in the thermal vibration spectrum of an $8 \times 2\mu\text{m}$ cantilever (Olympus BL-AC10DS) (see Supplementary Fig. 7a).

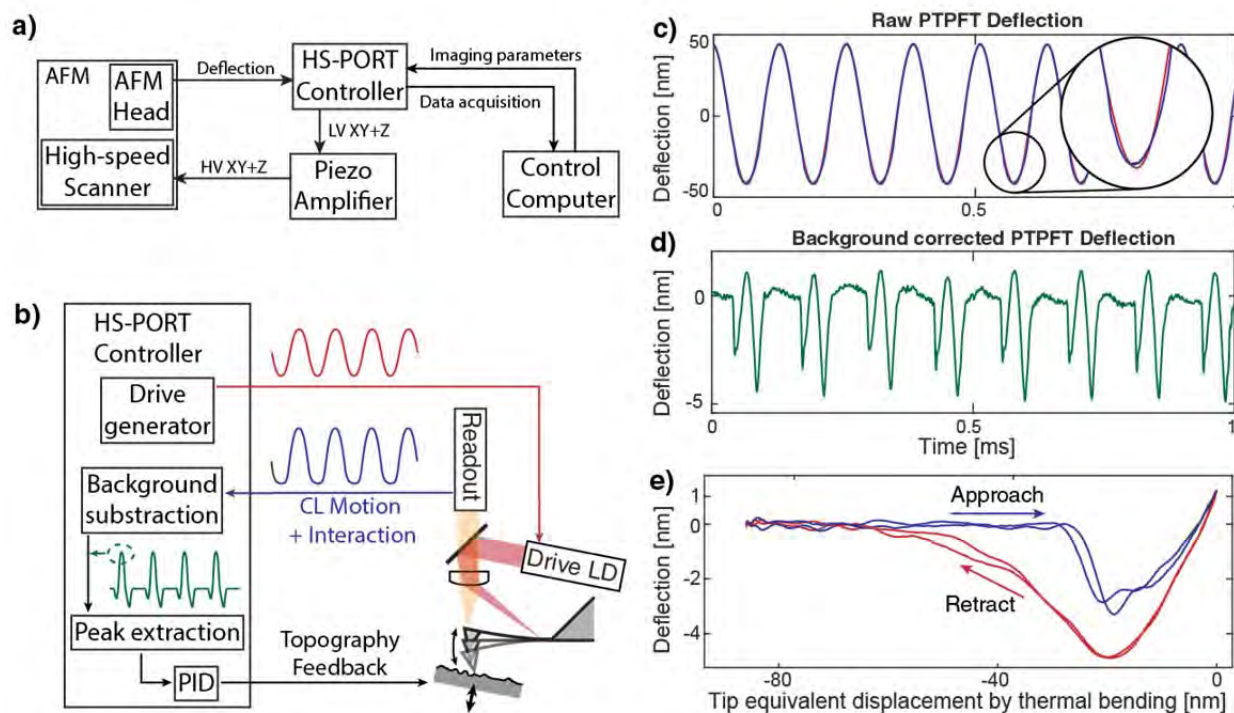


Supplementary Fig. 7: Performance of the home-built AFM. a) Thermal vibration spectrum of an AC-10DS cantilever, which is enabled by the very small spot size in combination with a custom high-speed readout. b) Section rendering of the built high-speed scanner, outlining the different actuators. c) Finite element simulation of the motion of the central flexure of the built high-speed scanner. d) Amplitude response curves for the z and x-y axes of the home-built high-speed scanner.

In addition to a fast, low-noise cantilever readout, high-speed AFM requires a scanner with high resonance frequencies. Based on the design by Fantner et al.⁴, we have built a miniaturized scanner compatible with the approach mechanism of the MultiMode base (see Supplementary Fig. 7b). The scanner is based on a titanium comb-flexure (Supplementary Fig. 7c) and allows for a motion of $1.8\mu\text{m}$ in x-y direction as well as of $\sim 2\mu\text{m}$ in z-direction. The high z-stiffness of the flexure design allows a high resonance frequency of over 100 kHz in z-direction, while allowing the x-y directions to remain sufficiently fast for high-speed imaging (Supplementary Fig. 7d). We use a commercial piezo-amplifier (Techproject Piezoamplifier) to drive the used stack piezo actuators.

4. Photothermal off-resonance controller

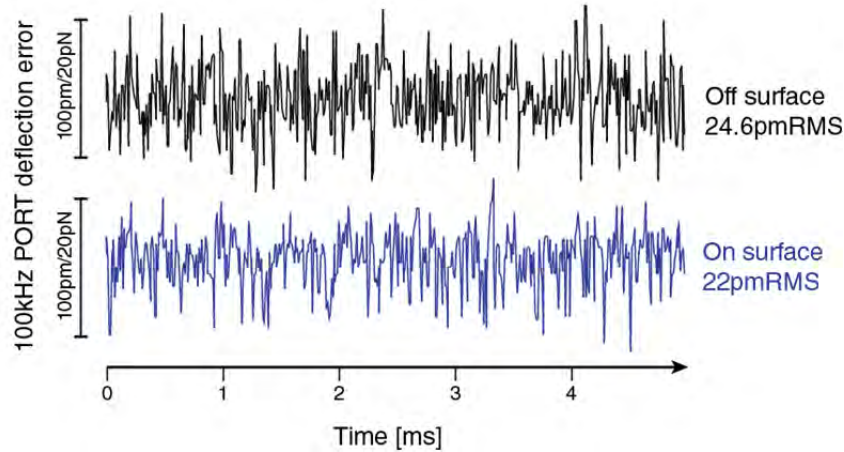
High-level description



Supplementary Fig. 8: Home-built photothermal off-resonance tapping (PORT) microscope. a) Wiring diagram of the set-up in PORT mode. b) Working principle of the PORT controller. A drive generator actuates the cantilever with either sinusoidal or piecewise sinusoidal motion components. The background is recorded with the surface slightly retracted and then subtracted from the input in real time. The resulting maximal interaction is then used as input to a PID controller. c) The raw signal from the photodetector for sinusoidal excitation, showing the small deviation created by the surface (blue) with respect to the unperturbed motion (red). d) The extracted tip-sample interaction distance after background subtraction. e) Reconstructed force-curve after background subtraction.

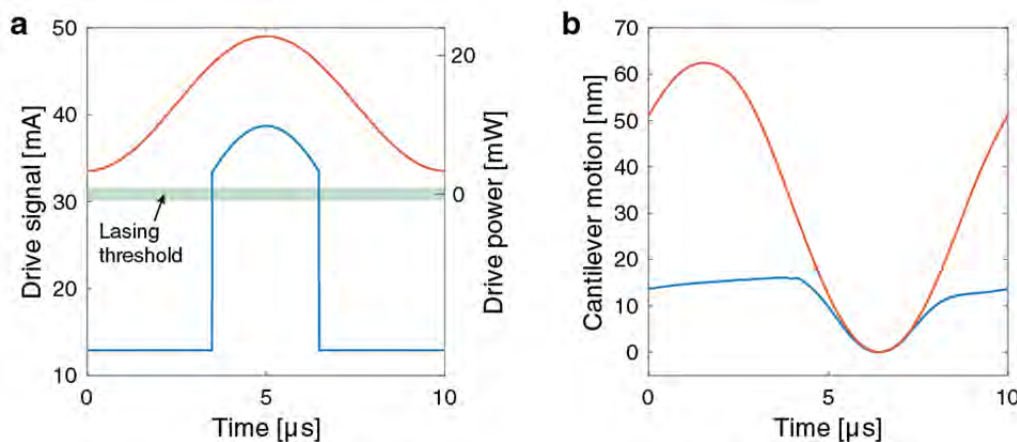
The working principle of the implemented controller is outlined in Supplementary Fig. 8. The controller does not need external devices for feedback, but requires a high-voltage amplifier for driving the scanner (Supplementary Fig. 8a). The PORT controller sends a drive signal, repeated at the rate of tapping, to the drive laser and records the resulting cantilever motion (Supplementary Fig. 8c). As with other force distance based imaging modes, it is in principle possible to extract material properties from the reconstructed PORT force curves. However, the short contact time and the fast loading rates will necessitate further understanding of the underlying process in order to be able to extract quantitative mechanical properties.

As the force calculations in figure 3 are highly averaged, the noise performance of the controller is not visible. The typical noise output performance of the force detection on an AC10DS cantilever is shown in Supplementary Fig. 9. The PORT noise at 100kTaps/s is recorded at the full 100kSps, as calculated in the controller, once for when the cantilever is able to move freely in the buffer and once when it is in feedback (intermittent contact with the surface).



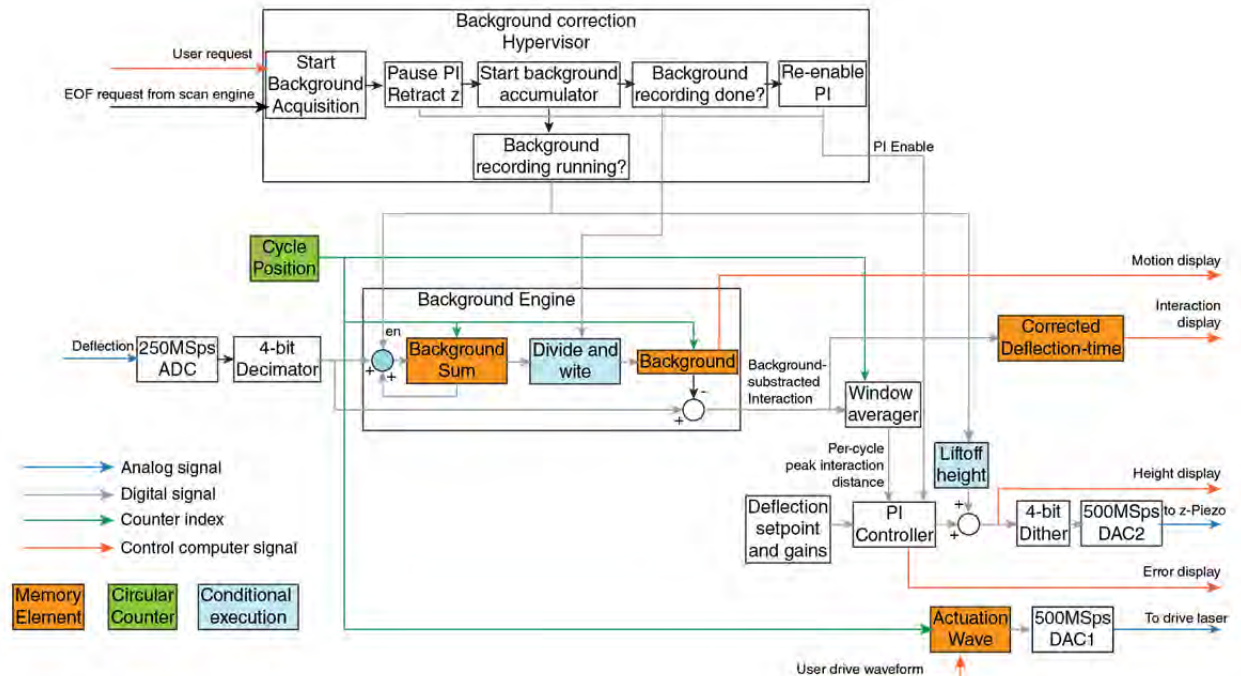
Supplementary Fig. 9: Point-by-point 100kHz PORT deflection error signal in buffer as obtained from the controller when retracted (top) and when in feedback with the surface (bottom). Note that the force noise that is dominated by the cantilever thermal noise is reduced slightly when the cantilever goes into contact with the surface.

78 The background motion resulting from the actuation is corrected regularly either manually or
 79 automatically at the end of an image to account for drifts in the detector or tip contaminations. For this,
 80 the feedback is temporarily disabled and the piezo retracted between 5-100nm. The cantilever motion,
 81 now free of any short-range surface interactions, is acquired over a number of periods and averaged,
 82 and finally the feedback is re-enabled. This motion is then subtracted from the input, after which the
 83 resulting waveform only contains components that arise from interaction with the surface. At the point
 84 where the recorded background interaction is lowest, the cantilever will touch the surface. There, a
 85 characteristic sinusoidal “heartbeat” appears in the signal (Supplementary Fig. 8d), from which a full
 86 force-curve can be reconstructed (Supplementary Fig. 8e). A number of points around the centre of this
 87 heartbeat are averaged in real time and used as input to the PI controller (Supplementary Fig. 8b).
 88



Supplementary Fig. 10: The drive signal in HS-PORT can be optimized to reduce heating on the cantilever. a) Instead of using a full sinusoidal drive (red), which keeps the laser on at all times, often a short pulse suffices (blue), especially if the cantilever is in a highly dampened environment. This reduces the time the laser is on, as well as the intensity of the light dramatically, together reducing heating. b) Resulting cantilever motion traces from sinusoidal heating (red) and pulsed heating (blue). The blue trace is almost identical to the red one close to the surface, but has less clearance further up. The

clearance can be adjusted to the needs of the experiment by increasing the laser power.



Supplementary Fig. 11: Low-level programming diagram of implemented controller.

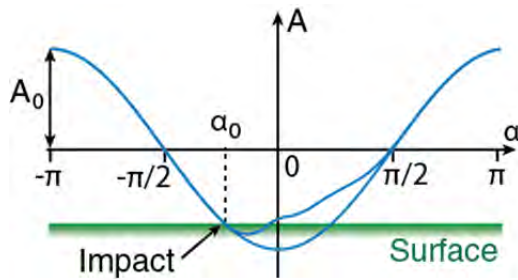
93 An in-depth description of the programming used in the implementation of the HS-PORT controller can
94 be seen in Supplementary Fig. 11. The controller consists of a constantly-executing part that handles
95 real-time data processing. A hypervisor controls the real-time part for the (programmatically rare) case
96 that a new background correction is requested.

The controller continuously outputs a user defined drive waveform directly to the actuation laser-driver at a frequency given by the number of points of the wave. The operation frequency of the implemented controller is 67.5MHz. The drive actuation generates a motion of the cantilever in the AFM, which is measured as a deflection. That deflection input is sampled with a 250MS/s analog-to-digital converter. The digital deflection is then decimated by a factor 4 to increase the input resolution from the native 16-bit DAC to 18-bit. In normal operation, a recorded background value at that position in the measurement cycle is then subtracted from the digitalized deflection. In each measurement cycle, there is a window of time in which the tip-surface interaction is anticipated to happen (e.g. the lowest point in the recorded cantilever motion), which is very constant per measurement frequency. The windowed average extracts the peak interaction distance for each surface interrogation cycle and sends it as a control input to the PI controller. The set-point distance (proportional to the set-point force) is subtracted from the peak interaction and a new height-output is computed based on the current integrator state and the new input. This output is then sent to a 4-bit dither, which modulates the output at high frequency to increase the output resolution of the digital-to-analog converter DAC2, which drives the output to the z-piezo-amplifier.

In case the controller receives a request for a reset of the background subtraction on the background correction hypervisor, the PI controller is paused and a liftoff-height is added to the z-output, effectively retracting the surface a small distance from the cantilever. A user-defined power-of-two number (typically between 1024-4092 cycles) of cycles of the deflection is then accumulated into the “Background Sum” memory. When the requested number of cycles is reached, the “Background Sum” memory is divided by the number of recorded cycles and written to the background memory, which then contains one highly averaged (and noise-free) background motion. That background memory is then used to subtract the background from the acquired deflection signal, thus returning to normal feedback operation. As a final step, the background correction hypervisor re-enables the PI controller so that tracking is restored.

5. Derivation of impact force scaling

For a highly dampened sinusoidally driven spring-mass system, the trajectory will usually largely recover to the unperturbed motion during one cycle if locally perturbed⁵. We therefore ignore in first approximation any resonance enhancement effects.



Supplementary Fig. 12: Sketch of cantilever impact trajectory. The cantilever with a free cosinusoidal motion of amplitude A_0 periodically impacts at a relative impact angle α_0 with the surface.

If the unperturbed motion at measurement frequency ω_m is given as

$$d(t) = -A_0 \cdot \cos(\omega_m t)$$

and the impact happens periodically at a relative impact angle α_0 (0 at the lowest point of the curve, $-\frac{\pi}{2}$ if it impacts at the highest speed, see Supplementary Fig. 12) we can write the tip velocity at the periodic time of impact t_{impact} as

$$v_i = A_0 \cdot \omega_m \cdot \sin(\omega_m t_{\text{impact}} + n \cdot 2\pi) = A_0 \cdot \omega_m \cdot \sin(\alpha_0) \quad (1)$$

Using the effective mass

$$m_{\text{eff}} = \frac{k}{\omega_{\text{res}}^2} \quad (2)$$

with the spring constant k and the resonant angular frequency cantilever ω_{res} ⁶. The cantilever impulse at impact is

$$p_i = m_{\text{eff}} \cdot v_i = \frac{k}{\omega_{\text{res}}^2} A_0 \cdot \omega_m \cdot \sin(\alpha_0)$$

135 We approximate the impact of the tip as frictionless elastic, as assumed by Hertz contact theory.
 136 Johnson⁷ (p. 353) gives the maximum deformation during Hertzian impact of two spheres of elastic
 137 modulus E^* with radii R_1 and R_2 and masses m_1 and m_2 colliding at an initial velocity V_z as

$$\delta_z^* = \left(\frac{15mV_z^2}{16R^{\frac{1}{2}}E^*} \right)^{\frac{2}{5}} \quad (3)$$

138 and the corresponding force between the spheres (p. 352) as

$$P = \frac{4}{3} R^{\frac{1}{2}} E^* \delta_z^{3/2} \quad (4)$$

139 where

$$\frac{1}{m} = \frac{1}{m_1} + \frac{1}{m_2} \quad \text{and} \quad \frac{1}{R} = \frac{1}{R_1} + \frac{1}{R_2}$$

140 To get the sphere-on-surface case, we assume the second sphere has infinite radius and infinite mass. As
 141 such we use the effective mass (2) of the cantilever as mass

$$m = m_{\text{eff}}$$

142 and R as the (constant) radius of the tip. Then the peak collision force P^* is calculated by substituting (3)
 143 into (4)

$$P^* = \frac{4}{3} R^{\frac{1}{2}} E^* (\delta_z^*)^{\frac{3}{2}} = \frac{4}{3} R^{\frac{1}{2}} E^* \left(\frac{15mV_z^2}{16R^{\frac{1}{2}}E^*} \right)^{\frac{3}{5}} = \frac{30^{\frac{3}{5}}}{6} (RE^{*2}m^3V_z^6)^{\frac{1}{5}} \quad (5)$$

144 Further substituting (1) and (2) into (5) gives the impact force scaling for an oscillating cantilever with
 145 periodic impact on the surface.

$$P^* = \frac{30^{\frac{3}{5}}}{6} \left(RE^{*2} \frac{k}{\omega_{\text{res}}^6} A_0^6 \omega_m^6 \sin^6 \alpha_0 \right)^{\frac{1}{5}} \quad (6)$$

146 Since R and E^* are constants for the same tip and the same sample, the scaling of the tip sample force
 147 can be rewritten in the proportionality relation

$$P^* \propto k^{\frac{3}{5}} \cdot \left(\frac{\omega_m}{\omega_{\text{res}}} A_0 \sin \alpha_0 \right)^{\frac{6}{5}} = k^{\frac{3}{5}} \cdot \left(\frac{f_m}{f_{\text{res}}} A_0 \sin \alpha_0 \right)^{\frac{6}{5}}$$

148 In practice, tip-sample interactions are generally not free of attractive forces⁸, as assumed when using
 149 Hertz contact mechanics. This is especially true when attractive electrostatic forces are present, which
 150 lead to the characteristic snap-in⁹. It is likely that such forces could lead to additional accelerations and,
 151 consequently, to different impact forces than are predicted by the simple model derived here.

In our simplified model, we assume critical damping. Amo et al.¹⁰ have studied the effect of damping on the accuracy of the measured peak force and adhesion in fast force mapping. They predict that the real repulsive interaction forces measured during an ORT cycle can deviate up by over 30% from what is observed on a deflection signal when using a cantilever in a low damping environment. This effect becomes increasingly important as the measurement frequency gets closer to the resonance frequency of the cantilever. However the magnitude of this effect decreases to below 6% when using a highly damped cantilever ($Q=1$)¹⁰. These authors further show that the property that is most affected by a higher measurement frequency relative to the resonance frequency of the cantilever is adhesion¹⁰. The short interaction times in HS-PORT lead to small adhesive forces¹¹. Therefore, we expect the dominating tip-sample force contribution for HS-PORT to be the repulsive forces from the initial impact, as well as the static contribution that is used as a control signal

References

1. Adams, J. D. *et al.* High-speed imaging upgrade for a standard sample scanning atomic force microscope using small cantilevers. *Rev. Sci. Instrum.* **85**, 93702 (2014).
2. Nievergelt, A. P., Adams, J. D., Odermatt, P. D. & Fantner, G. E. High-frequency multimodal atomic force microscopy. *Beilstein J. Nanotechnol.* **5**, 2459–2467 (2014).
3. Enning, R. *et al.* A high frequency sensor for optical beam deflection atomic force microscopy. *Rev. Sci. Instrum.* **82**, 43705 (2011).
4. Fantner, G. E. *et al.* Components for high speed atomic force microscopy. *Ultramicroscopy* **106**, 881–7 (2006).
5. Basak, S. & Raman, A. Dynamics of tapping mode atomic force microscopy in liquids: Theory and experiments. *Appl. Phys. Lett.* **91**, (2007).
6. Xu, X., Carrasco, C., de Pablo, P. J., Gomez-Herrero, J. & Raman, A. Unmasking imaging forces on soft biological samples in liquids when using dynamic atomic force microscopy: a case study on viral capsids. *Biophys. J.* **95**, 2520–8 (2008).
7. Johnson, K. L. *Contact Mechanics*. Cambridge University Press **108**, (Cambridge University Press, 1985).
8. Guzman, H. V., Perrino, A. P. & Garcia, R. Peak forces in high-resolution imaging of soft matter in liquid. *ACS Nano* **7**, 3198–3204 (2013).
9. García, R. & San Paulo, A. Attractive and repulsive tip-sample interaction regimes in tapping-mode atomic force microscopy. *Phys. Rev. B* **60**, 4961–4967 (1999).
10. Amo, C. A. & Garcia, R. Fundamental High-Speed Limits in Single-Molecule, Single-Cell, and Nanoscale Force Spectroscopies. *ACS Nano* **10**, 7117–7124 (2016).
11. Van Der Werf, K. O., Putman, C. A. J., De Grooth, B. G. & Greve, J. Adhesion force imaging in air and liquid by adhesion mode atomic force microscopy. *Appl. Phys. Lett.* **65**, 1195–1197 (1994).